

Fixing the Residual Flattening of an Upwind Compact Scheme for Steady Incompressible Flows in Enclosed Domains

Yunchu Wang and Li Yuan*

*LSEC, Institute of Computational Mathematics and Scientific/Engineering Computing, Academy of Mathematics and Systems Science, Chinese Academy of Sciences, Beijing 100190, China.
School of Mathematical Sciences, University of Chinese Academy of Sciences, Beijing 100190, China.*

Received 28 November 2020; Accepted (in revised version) 6 April 2021.

Abstract. The iterative convergence of the upwind compact finite difference scheme for the artificial compressibility method [A. Shah *et al.*, A third-order upwind compact scheme on curvilinear meshes for the incompressible Navier-Stokes equations, *Commun. Comput. Phys.* **5** (2009)] is studied. It turns out that for steady flows in enclosed domains the residuals do not converge to machine zero. The reason is a non-uniqueness of the calculated pressure in the case where Neumann boundary conditions for the pressure are imposed on all boundaries. The problem can be fixed by modifying the derivatives of mass flux obtained from the upwind compact scheme to satisfy the global mass conservation constraint. Numerical tests show that with this modification the scheme converges to machine zero with the original third-order accuracy.

AMS subject classifications: 76D05, 65M06

Key words: Incompressible Navier-Stokes equations, artificial compressibility, upwind compact difference, convergence, enclosed domain.

1. Introduction

The artificial compressibility (AC) method was proposed by Chorin [6] for the numerical solution of the incompressible Navier-Stokes equations. In this method, a pseudo-time derivative of pressure is added to the continuity equation, so that the original elliptic-parabolic system of equations become hyperbolic in time. After that, various well-established compressible flow numerical algorithms can be used in the AC method. The AC method was initially used to compute steady flows with the approximate factorisation algorithms [20, 32]. Later it was extended to unsteady incompressible flows [2, 34, 41] by using the

*Corresponding author. *Email addresses:* ycwang@lsec.cc.ac.cn (Y. C. Wang), lyuan@lsec.cc.ac.cn (L. Yuan)

dual time stepping technique [5, 16]. Meanwhile, high-resolution total variation diminishing (TVD) schemes [15] and high-order flux difference splitting (FDS)-based upwind schemes [33–35] were introduced in conjunction with the lower-upper symmetric Gauss-Seidel (LU-SGS) scheme [44], line Gauss-Seidel relaxation scheme [33,34] and generalised minimal residual (GMRES) algorithm [13, 31]. The influence of the artificial pressure wave of the hyperbolic system on convergence of the AC method was analysed by Kwak *et al.* [20, 21]. Recently, high-order discontinuous Galerkin schemes have been also incorporated in this method [48].

Compact finite difference schemes attracted substantial attention since they have lower truncation errors and higher spectral resolution than non-compact ones [22]. For compressible flows such methods are often employed in combination with weighted essentially non-oscillatory (WENO) schemes [18] in order to deal with shock waves. Thus Deng [7] developed a WENO reconstruction-based compact nonlinear scheme, Jiang *et al.* [17] considered a WENO-weighted compact difference scheme, and Pirozzoli [27] and Ren *et al.* [28] worked with conservative compact reconstruction-WENO hybrid schemes, to mention a few. These methods have better accuracy and resolution than stand-alone WENO schemes. For incompressible flows, the solutions of the corresponding equations have no strong discontinuities, so that any linearly stable compact scheme can be exploited. In particular, central compact schemes with implicit central filtering [43] are applied to the AC method [8, 29, 47]. The FDS scheme [30] is a full wave approximate Riemann solver for the compressible Euler equations and can capture shear waves accurately. Following the successful application of FDS-based high-order upwind schemes in incompressible flow simulations [33–35], Shah *et al.* [37, 38] developed FDS-based third- and fifth-order upwind compact schemes, and demonstrated their superior spectral resolution over the FDS-based non-compact upwind schemes of same order [39].

However, the authors of this work discovered that although for steady flows in enclosed domain the residuals of the conservative non-compact upwind schemes of [33–35] converge to machine zero, the nonconservative third-order upwind compact schemes of [37, 38] converge to a number much greater than machine zero. In monitoring the convergence history of the flow variables of the scheme [37] for steady flows in enclosed domain, we noted that the velocity increments converge to machine zero but the pressure increments converge to a number much greater than machine zero. The reason is the non-uniqueness of the pressure in enclosed domains, and we emphasize that this has an adverse impact on the convergence of the pressure time derivative term in the continuity equation of the AC method. In order to fix the problem, we use modified numerical derivatives of the mass flux to satisfy the global mass conservation constraint. Numerical examples show that the residuals of the modified upwind compact scheme for steady flows in enclosed domain converge to machine zero with the third-order accuracy.

The rest of the paper is organised as follows. Section 2 reviews the governing equations and FDS-based third-order upwind compact scheme. The convergence of this scheme for steady flows is tested and analysed in Section 3, and a modification of the residual stall is suggested in Section 4. Benchmark examples in Section 5 show the effectiveness of the modified scheme. Finally, our conclusion is given in Section 6.

2. Governing Equations and an Upwind Compact Scheme

Here we consider two-dimensional equations but the extension to three dimensions is straightforward. The governing equations of the AC method are the incompressible Navier-Stokes equations with the time derivative of the pressure in the continuity equation — i.e.

$$\frac{\partial \mathbf{Q}}{\partial \tau} + \frac{\partial(\mathbf{E} - \mathbf{E}_v)}{\partial x} + \frac{\partial(\mathbf{F} - \mathbf{F}_v)}{\partial y} = 0, \quad (x, y) \in \Omega, \quad \tau \geq 0, \quad (2.1)$$

where x, y are the Cartesian coordinates, τ is the time, and Ω the solution domain. The solution vector \mathbf{Q} , inviscid flux vectors \mathbf{E}, \mathbf{F} , and viscous flux vectors $\mathbf{E}_v, \mathbf{F}_v$ have the form

$$\mathbf{Q} = \begin{bmatrix} p \\ u \\ v \end{bmatrix}, \quad \mathbf{E} = \begin{bmatrix} \beta u \\ u^2 + p \\ uv \end{bmatrix}, \quad \mathbf{F} = \begin{bmatrix} \beta v \\ uv \\ v^2 + p \end{bmatrix}, \quad \mathbf{E}_v = \frac{1}{Re} \begin{bmatrix} 0 \\ u_x \\ v_x \end{bmatrix}, \quad \mathbf{F}_v = \frac{1}{Re} \begin{bmatrix} 0 \\ u_y \\ v_y \end{bmatrix}, \quad (2.2)$$

where β is the artificial compressibility factor, p is the pressure, u, v are the velocity components, and Re is the Reynolds number. It is easily seen that if $\partial \mathbf{Q} / \partial \tau \rightarrow 0$, the Eqs. (2.1) become the steady incompressible Navier-Stokes equations. The Jacobian matrices \mathbf{A} and \mathbf{B} of the inviscid flux vectors and \mathbf{A}_v and \mathbf{B}_v of the viscous flux vectors are

$$\mathbf{A} = \frac{\partial \mathbf{E}}{\partial \mathbf{Q}} = \begin{bmatrix} 0 & \beta & 0 \\ 1 & 2u & 0 \\ 0 & v & u \end{bmatrix}, \quad \mathbf{B} = \frac{\partial \mathbf{F}}{\partial \mathbf{Q}} = \begin{bmatrix} 0 & 0 & \beta \\ 0 & v & u \\ 1 & 0 & 2v \end{bmatrix}, \quad (2.3)$$

and

$$\mathbf{A}_v = \frac{\partial \mathbf{E}_v}{\partial \mathbf{Q}} = \frac{\mathbf{I}_m}{Re} \frac{\partial}{\partial x}, \quad \mathbf{B}_v = \frac{\partial \mathbf{F}_v}{\partial \mathbf{Q}} = \frac{\mathbf{I}_m}{Re} \frac{\partial}{\partial y} \quad \text{with} \quad \mathbf{I}_m = \begin{bmatrix} 0 & 0 & 0 \\ 0 & 1 & 0 \\ 0 & 0 & 1 \end{bmatrix}.$$

The matrices \mathbf{A} and \mathbf{B} are diagonalisable with real eigenvalues — i.e.

$$\mathbf{A} = \mathbf{X} \mathbf{\Lambda}_A \mathbf{X}^{-1}, \quad \mathbf{B} = \mathbf{Y} \mathbf{\Lambda}_B \mathbf{Y}^{-1},$$

where

$$\begin{aligned} \mathbf{\Lambda}_A &= \text{diag}(u, u + c_1, u - c_1), & c_1 &= \sqrt{u^2 + \beta}, \\ \mathbf{\Lambda}_B &= \text{diag}(v, v + c_2, v - c_2), & c_2 &= \sqrt{v^2 + \beta}, \\ \mathbf{X} &= \begin{bmatrix} 0 & c_1(c_1 - u) & c_1(c_1 + u) \\ 0 & c_1 & -c_1 \\ 1 & v & v \end{bmatrix}, & \mathbf{X}^{-1} &= \frac{1}{c_1^2} \begin{bmatrix} -v & -uv & c_1^2 \\ \frac{1}{2} & \frac{1}{2}(c_1 + u) & 0 \\ \frac{1}{2} & -\frac{1}{2}(c_1 - u) & 0 \end{bmatrix}, \\ \mathbf{Y} &= \begin{bmatrix} 0 & c_2(c_2 - v) & c_2(c_2 + v) \\ 1 & u & u \\ 0 & c_2 & -c_2 \end{bmatrix}, & \mathbf{Y}^{-1} &= \frac{1}{c_2^2} \begin{bmatrix} -u & c_2^2 & -uv \\ \frac{1}{2} & 0 & \frac{1}{2}(c_2 + v) \\ \frac{1}{2} & 0 & -\frac{1}{2}(c_2 - v) \end{bmatrix}. \end{aligned}$$

Approximating the time derivative in (2.1) by the backward Euler difference yields

$$\frac{\mathbf{Q}^{m+1} - \mathbf{Q}^m}{\Delta\tau} + \left[\frac{\partial(\mathbf{E} - \mathbf{E}_v)}{\partial x} + \frac{\partial(\mathbf{F} - \mathbf{F}_v)}{\partial y} \right]^{m+1} = 0. \tag{2.4}$$

Setting $\Delta\mathbf{Q}^m = \mathbf{Q}^{m+1} - \mathbf{Q}^m$ and using Taylor series expansions

$$\begin{aligned} \mathbf{E}^{m+1} &\approx \mathbf{E}^m + \mathbf{A}^m \Delta\mathbf{Q}^m, \\ \mathbf{E}_v^{m+1} &\approx \mathbf{E}_v^m + \mathbf{A}_v^m \Delta\mathbf{Q}^m \end{aligned}$$

for the linearisation of the fluxes at $(m + 1)$ -th time level with respect to m -th level, we get the delta form of the Eq. (2.4)

$$\begin{aligned} &\left\{ \mathbf{I} + \Delta\tau \left[\frac{\partial(\mathbf{A}^m - \mathbf{A}_v^m)}{\partial x} + \frac{\partial(\mathbf{B}^m - \mathbf{B}_v^m)}{\partial y} \right] \right\} \Delta\mathbf{Q}^m \\ &= -\Delta\tau \left[\frac{\partial(\mathbf{E} - \mathbf{E}_v)}{\partial x} + \frac{\partial(\mathbf{F} - \mathbf{F}_v)}{\partial y} \right]^m \equiv -\mathbf{R}^m. \end{aligned} \tag{2.5}$$

Applying the approximate factorisation technique [20] to the left-hand side of the Eq. (2.5), we arrive at the alternating direction implicit scheme

$$\left[\mathbf{I} + \Delta\tau \left(\delta_x^- \mathbf{A}^+ + \delta_x^+ \mathbf{A}^- - \frac{\mathbf{I}_m}{Re} \delta_x^2 \right) \right] \left[\mathbf{I} + \Delta\tau \left(\delta_y^- \mathbf{B}^+ + \delta_y^+ \mathbf{B}^- - \frac{\mathbf{I}_m}{Re} \delta_y^2 \right) \right] \Delta\mathbf{Q}^m = -\mathbf{R}^m, \tag{2.6}$$

where

$$\begin{aligned} \mathbf{A}^\pm &= \frac{1}{2} [\mathbf{A} \pm \rho(\mathbf{A})\mathbf{I}], \quad \rho(\mathbf{A}) = \kappa \max_{1 \leq l \leq 3} (|\Lambda_A(l)|), \quad \kappa \geq 1.0, \\ \delta_x^+ f_i &= \frac{f_{i+1} - f_i}{\Delta x}, \quad \delta_x^- f_i = \frac{f_i - f_{i-1}}{\Delta x}, \quad \delta_x^2 f_i = \frac{f_{i+1} - 2f_i + f_{i-1}}{\Delta x^2}, \end{aligned}$$

and the second factor in the left-hand side of (2.6) is defined analogously.

In order to obtain block tridiagonal equations in each direction, the viscous terms in the Eq. (2.6) are discretised by the second-order central difference and the convective terms in the left-hand by the first-order upwind difference. But a FDS-based third-order upwind compact scheme is used in the right-hand side of (2.6), which is described below.

The convective terms in the right-hand side of the Eq. (2.6) are computed as $(\partial\mathbf{E}/\partial x)_i = (\partial\mathbf{E}^+/\partial x)_i + (\partial\mathbf{E}^-/\partial x)_i$ with the split derivatives $(\partial\mathbf{E}^\pm/\partial x)_i$ at the grid points i determined by the FDS-based third-order upwind compact scheme [37, 38]. The scheme is originated from the upwind compact difference scheme [11] when the left-hand side contains two unknown split derivatives at two consecutive grid points and the right-hand side the differences of grid point values of split flux functions. These differences can be determined by Roe's FDS technique as

$$\Delta\mathbf{E}_{i+\frac{1}{2}}^\pm \equiv \mathbf{E}_{i+1}^\pm - \mathbf{E}_i^\pm = \mathbf{A}^\pm \left(\bar{\mathbf{Q}}_{i+\frac{1}{2}} \right) (\mathbf{Q}_{i+1} - \mathbf{Q}_i),$$

where

$$A^\pm(Q) = X(Q)\Lambda_A^\pm(Q)X^{-1}(Q).$$

We remark that for incompressible flows, the arithmetic average $\bar{Q}_{i+1/2} = (Q_i + Q_{i+1})/2$ satisfies the Roe property $\Delta E = A(\bar{Q})\Delta Q$ exactly. This follows directly from the vector E in (2.2) and the matrix A in (2.3). For all interior points $i = 1, \dots, N - 1$, the third-order upwind compact scheme has the form

$$\begin{aligned} \frac{2}{3} \frac{\partial E^+}{\partial x} \Big|_i + \frac{1}{3} \frac{\partial E^+}{\partial x} \Big|_{i-1} &= \frac{5\Delta E_{i-1/2}^+ + \Delta E_{i+1/2}^+}{6\Delta x} + \mathcal{O}(\Delta x^3), \quad i = 1, \dots, N - 1, \\ \frac{2}{3} \frac{\partial E^-}{\partial x} \Big|_i + \frac{1}{3} \frac{\partial E^-}{\partial x} \Big|_{i+1} &= \frac{\Delta E_{i-1/2}^- + 5\Delta E_{i+1/2}^-}{6\Delta x} + \mathcal{O}(\Delta x^3), \quad i = N - 1, \dots, 1. \end{aligned} \tag{2.7}$$

To solve Eq. (2.7), an explicit, dissipative, and third-order one-sided boundary scheme is used at the boundary points $i = 0$ and $i = N$, viz.

$$\begin{aligned} \frac{\partial E^+}{\partial x} \Big|_{i=0} &= \frac{-11E_i^+ + 18E_{i+1}^+ - 9E_{i+2}^+ + 2E_{i+3}^+}{6\Delta x} + \mathcal{O}(\Delta x^3) \\ &= \frac{11\Delta E_{i+1/2}^+ - 7\Delta E_{i+3/2}^+ + 2\Delta E_{i+5/2}^+}{6\Delta x} + \mathcal{O}(\Delta x^3), \\ \frac{\partial E^-}{\partial x} \Big|_{i=N} &= \frac{-2E_{i-3}^- + 9E_{i-2}^- - 18E_{i-1}^- + 11E_i^-}{6\Delta x} + \mathcal{O}(\Delta x^3) \\ &= \frac{2\Delta E_{i-5/2}^- - 7\Delta E_{i-3/2}^- + 11\Delta E_{i-1/2}^-}{6\Delta x} + \mathcal{O}(\Delta x^3). \end{aligned} \tag{2.8}$$

The Eqs. (2.7) are then solved by marching forward/backward to get all positive/negative derivatives starting from the boundary derivative (2.8) at $i = 0$ and $i = N$, respectively. On a symmetric or open boundary, Eqs. (2.8) are replaced by the classical third-order upwind difference schemes using known ghost points outside the boundaries — i.e.

$$\begin{aligned} \frac{\partial E^+}{\partial x} \Big|_{i=0} &\approx \frac{E_{i-2}^+ - 6E_{i-1}^+ + 3E_i^+ + 2E_{i+1}^+}{6\Delta x} = \frac{-\Delta E_{i-3/2}^+ + 5\Delta E_{i-1/2}^+ + 2\Delta E_{i+1/2}^+}{6\Delta x}, \\ \frac{\partial E^-}{\partial x} \Big|_{i=N} &\approx \frac{-2E_{i-1}^- - 3E_i^- + 6E_{i+1}^- - E_{i+2}^-}{6\Delta x} = \frac{2\Delta E_{i-1/2}^- + 5\Delta E_{i+1/2}^- - \Delta E_{i+3/2}^-}{6\Delta x}. \end{aligned}$$

For periodic boundaries, a periodic bi-diagonal solver similar to the tri-diagonal solver [25] is used to solve the corresponding periodic bi-diagonal system (2.7).

It is well known that the incompressible Navier-Stokes equations with Neumann boundary conditions for the pressure on all boundaries admit a non-unique pressure up to a constant. To remove the constant in the numerical solution as convention [10], we subtract a reference pressure (the pressure at any fixed reference point or the averaged pressure of the whole domain) from the calculated pressure field $\tilde{p}(i, j)$ after each time step — i.e.

$$p^{m+1}(i, j) = \tilde{p}^{m+1}(i, j) - \tilde{p}^{m+1}(i_{\text{ref}}, j_{\text{ref}}), \quad \forall i, j \in \Omega. \tag{2.9}$$

However, we discovered that the residual $\|\mathbf{R}^m/\Delta\tau\|_2$, can not converge to machine zero. This is shown in Section 3 and a simple modification to fix this problem is proposed in Section 4.

3. Convergence of an Upwind Compact Scheme for Steady State

In this section, we first test the residual convergence of the original third-order upwind compact scheme (2.7)-(2.8) for steady flows in open and enclosed domains respectively, then we analyse why the convergence differs significantly between open and enclosed domains.

3.1. Convergence tests

We choose the plane Couette-Poiseuille flow (open domain, in which the fluid has inlet and outlet boundaries) and lid-driven cavity flow (enclosed domain, in which the fluid does not go through boundaries of the domain) as test cases. For the plane Couette-Poiseuille flow, non-slip conditions for the velocity and Neumann boundary conditions for the pressure derived from the y -component momentum equation are used on the upper and lower plates. The pressure gradient on either plate is discretised with third order one-sided finite differences similar to Eq. (2.8). The zero transverse velocity component and the zero normal gradient of the streamwise velocity component are used on the inlet and the zero normal gradients of both velocity components are used on the outlet. The pressure at the outlet is set to zero while the pressure at the inlet is specified by the dimensionless constant pressure gradient $\Pi = -Re\partial p/\partial x$ [37]. For the lid-driven cavity flow, the velocity on the top lid along the x -direction is set to 1 while velocities on all other walls are zero. A Neumann boundary condition derived from the momentum equation normal to a wall is used for the pressure. Furthermore, the averaged pressure of the whole domain as the reference pressure is subtracted from the computed pressures in each iteration. In both tests we use the computational domain $[0, 1] \times [0, 1]$, the mesh with 129×129 uniformly distributed grid points, the artificial compressibility factor $\beta = 10$, and local time steps determined with CFL = 10.

Fig. 1 shows convergence of the residuals $\|\mathbf{R}^m/\Delta\tau\|_2$ of Eq. (2.6) for the two test cases. Note that the residual for the plane Couette-Poiseuille flow converges to 10^{-11} , which is close to machine zero. For the lid-driven cavity flow the residual only diminishes to about 10^{-3} and then gets flat. Adjusting the artificial compressibility factor β , the CFL number or grid point number does not improve the convergence much. We remark that although for the lid-driven cavity flow the pressure field is corrected by the reference pressure as Eq. (2.9), the residual still does not converge to machine zero.

3.2. Analysis of convergence

Now we want to discuss the reason why for the lid-driven cavity flow, the original upwind compact scheme does not converge to machine zero. The distributions of the solution

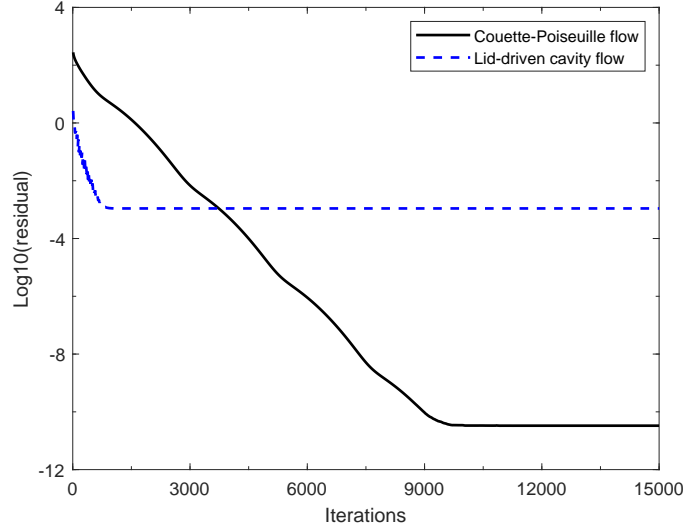


Figure 1: Convergence of original upwind compact scheme for plane Couette-Poiseuille flow (solid line) at $\Pi = 10$ and lid-driven cavity flow (dashed line) at $Re = 100$. Initial flow fields of interior points are $p = u = v = 0$.

increments $(\Delta p, \Delta u, \Delta v) = \Delta \mathbf{Q} = \mathbf{Q}^{m+1} - \mathbf{Q}^m$ at 5000 iterations are shown in the first three frames in Fig. 2. We note that Δu and Δv are close to 10^{-16} , while Δp is close to 10^{-5} . However, if we consider $\Delta p' = \Delta p - \Delta p_{\text{ref}}$, where Δp_{ref} is the value of Δp at a fixed reference point, then $\Delta p'$ is close to the machine zero — cf. the last frame in Fig. 2. $\Delta p' \rightarrow 0$ is equivalent to $\max_{i,j} |p_{i,j}^{m+1} - p_{i,j}^m - \Delta p_{\text{ref}}| \rightarrow 0$, which means that the pressure field is convergent up to a constant Δp_{ref} that may vary with time. Fig. 3 shows convergence of the residuals \mathbf{R} , the increments $\Delta \mathbf{Q}$ and the modified increments $\Delta \mathbf{Q}' = (\Delta p', \Delta u, \Delta v)$. We observe that \mathbf{R} drops to about 10^{-3} and $\Delta \mathbf{Q}$ to 10^{-5} , while $\Delta \mathbf{Q}'$ declines to 10^{-16} . Besides, for present implicit time scheme each component of the vector \mathbf{R} gets flat, whereas for the explicit time scheme, the residuals of the u and v momentum equations converge to machine zero while the residual of the continuity equation still gets flat.

These results hint that the residual does not converge to machine zero because the continuity equation in the AC method cannot converge to machine zero. This can be explained as follows. Since the Neumann boundary conditions for the pressure are used on all walls, the pressure is unique up to a constant in the steady-state solution of the incompressible Navier-Stokes equations. It can be uniquely defined by subtracting a reference pressure similar to (2.9). However, the reference pressure can change with time τ , $p(x, y, \tau) = p_{\text{steady}}(x, y) + p_{\text{ref}}(\tau)$, so that in the continuity equation (2.1) the time derivative of the pressure never vanishes. This defect is specific to the AC method. In most cases, the residuals converge to the magnitude of the spatial discretisation errors of the scheme and this does not affect the accuracy of the method. However, it is still advisable to make the residual converge to machine zero since it is an important indicator of steady state numerical solutions.

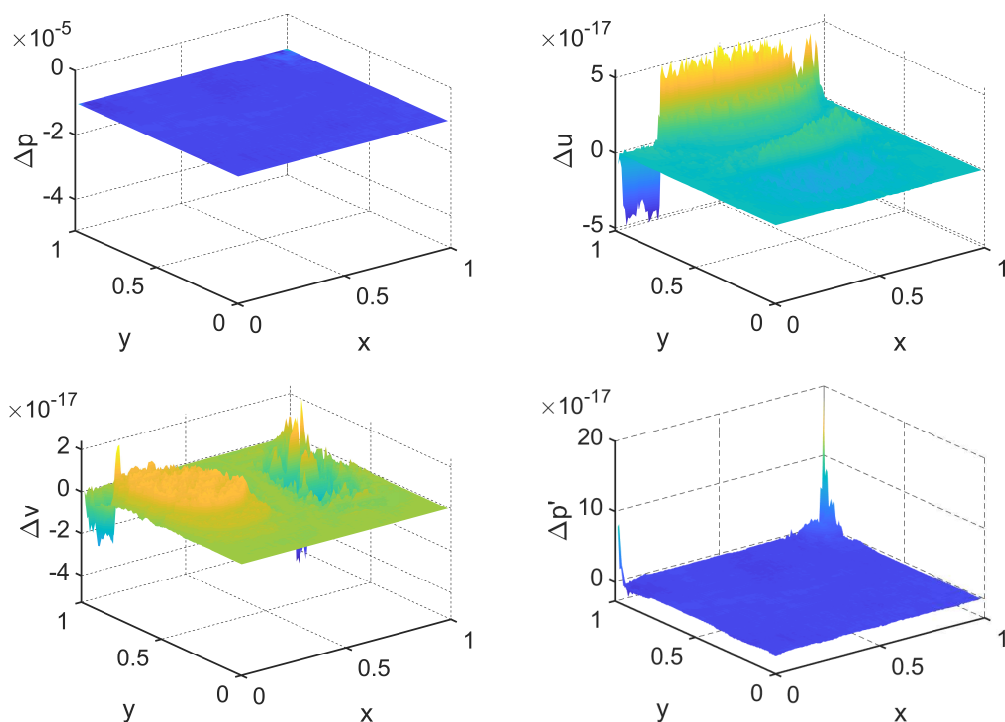


Figure 2: Distributions of solution increments $\Delta p, \Delta u, \Delta v$ and $\Delta p'$ at 5000 steps for lid-driven flow computed with the original upwind compact scheme, $Re = 100, \beta = 10, CFL = 10, 129 \times 129$ grid points.

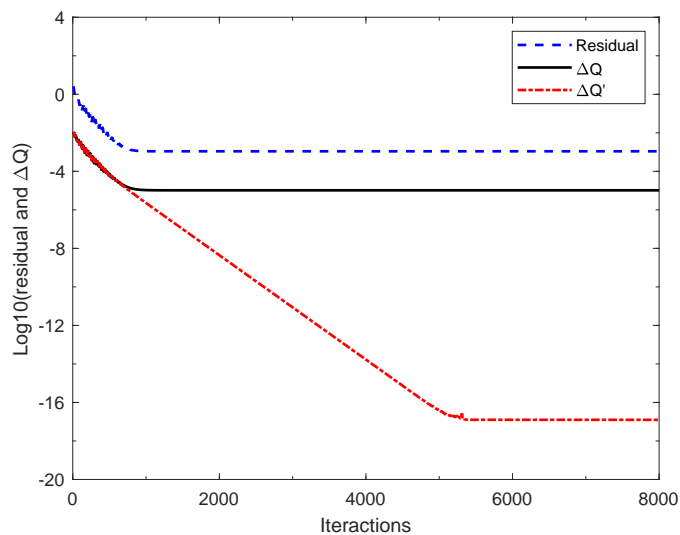


Figure 3: Convergence histories of residuals \mathbf{R} , increments $\Delta \mathbf{Q}$ and modified increments $\Delta \mathbf{Q}'$ for lid-driven cavity flow computed with the original upwind compact scheme at $Re = 100, \beta = 10, CFL = 10$, and 129×129 grid points.

4. A Simple Fix for Residual Stall

As is shown in Section 3, the pressure increment Δp does not converge to machine zero. This means that the mass conservation equation is not satisfied. In the plane Couette-Poiseuille flow, the normal velocity components on the inlet and outlet are allowed to change, so that they may cancel global mass conservation errors accumulated at the interior points. On the other hand, for cavity flows they are fixed and cannot respond to the mass conservation errors mentioned. This suggests that keeping the global conservation of mass in enclosed domain is critical for the residual convergence. Consider for example a grid line in the x -direction. The continuity equation of the AC method can be written in the following integral form:

$$\int_a^b \frac{\partial}{\partial \tau} p(x, \tau) dx = -(f(b, \tau) - f(a, \tau)), \quad (4.1)$$

where $[a, b]$ is an interval and f the mass flux function. Assume that this interval is divided in N equal subintervals by $N + 1$ grid points. Approximating the integral in (4.1) by a numerical quadrature [3, 22], we have

$$\Delta x \sum_{i=0}^N \omega_i \frac{\partial p_i}{\partial \tau} = -(f(b, \tau) - f(a, \tau)). \quad (4.2)$$

If the flow domain is enclosed, the right-hand side of (4.2) is zero. Using the finite difference equation $\partial p_i / \partial \tau = -f'_i$, and assuming that $\omega_0 = \omega_N = 0$ and $\omega_i = 1/(N - 1)$ for all interior points, the numerical derivatives of the mass flux f'_i , should satisfy the global mass conservation condition

$$\sum_{i=1}^{N-1} f'_i = 0. \quad (4.3)$$

In general, the terms f'_i determined by the scheme (2.7)-(2.8) do not satisfy the Eq. (4.3). Therefore, the derivatives f'_i are modified as follows:

$$f'_{i,\text{mod}} = f'_i - \frac{1}{N-1} \sum_{j=1}^{N-1} f'_j, \quad i = 1, \dots, N-1. \quad (4.4)$$

The method (2.7)-(2.8) combined with the terms (4.4) is called the modified upwind compact scheme. Fig. 4 shows the convergence of the lid-driven cavity flow computed using the modified upwind compact scheme. We note that the residuals converge to 10^{-12} , which is close to machine zero. In the next section, we provide other numerical examples to show that this simple modification can make the residuals converge to machine zero with the original accuracy.

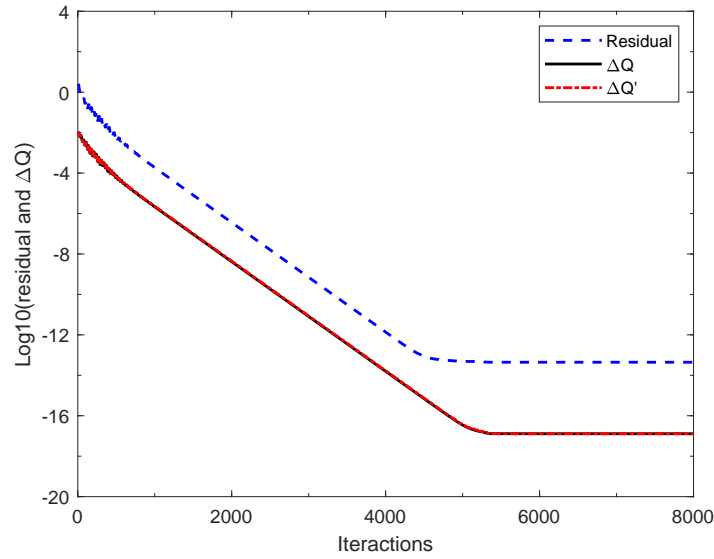


Figure 4: Convergence history of lid-driven cavity flow computed with the modified upwind compact scheme at $Re = 100$. $\beta = 10$, $CFL = 10$, and 129×129 grid points.

5. Numerical Results

In this section, several test problems demonstrate the effectiveness of the modified upwind compact scheme. In particular, we consider a modified lid-driven cavity flow, lid-driven rectangular cavity flows with different aspect ratios, and backward facing step flow problems. Finally, the spherical Couette flow is used to show both the convergence and simulation capability of the modified scheme.

5.1. Modified cavity flow

We use the modified lid-driven cavity flow problem [40] to examine the convergence and accuracy of the modified upwind compact scheme. The problem is considered in the square $0 \leq x, y \leq 1$. The lid is driven horizontally with the space-dependent body force

$$\begin{aligned}
 b(x, y) = & -\frac{8}{Re} \left[\left(8x^3 - 12x^4 + \frac{24}{5}x^5 \right) + (2x - 6x^2 + 4x^3)(24y^2 - 4) \right. \\
 & \left. + (24x - 12)(y^4 - y^2) \right] \\
 & - 64 \left\{ 0.5 \left[(x^2 - 2x^3 + x^4)^2 (-4y + 8y^3 - 24y^5) \right] \right. \\
 & \left. - (2y^3 - 6y^5 + 4y^7)(-2x^2 + 8x^3 - 14x^4 + 12x^5 - 4x^6) \right\}
 \end{aligned}$$

added to the left-hand side of the y -momentum equation of the Eqs. (2.1). This problem has the following analytic solution:

$$\begin{aligned} u(x, y) &= 8(x^2 - 2x^3 + x^4)(-2y + 4y^3), \\ v(x, y) &= -8(2x - 6x^2 + 4x^3)(-y^2 + y^4), \\ p(x, y) &= \frac{8}{Re} \left[\left(8x^3 - 12x^4 + \frac{24}{5}x^5 \right) y + (2x - 6x^2 + 4x^3)(-2y + 4y^3) \right] \\ &\quad + 64 \left(\frac{x^4}{2} - 2x^5 + 3x^6 - 2x^7 + \frac{x^8}{2} \right) \\ &\quad \times \left[-(-2y + 4y^3)^2 + (-2 + 12y^2)(-y^2 + y^4) \right]. \end{aligned}$$

On boundaries we impose Dirichlet conditions for the velocity and the Neumann conditions for the pressure. The normal derivatives of pressure in the Neumann conditions are approximated by the one-sided third-order boundary difference scheme (2.8). The initial conditions are zero for all flow variables. Steady state solutions are determined on a series of refined grids. The numerical order of accuracy is defined by

$$\text{Order} := \frac{\ln(e_2/e_1)}{\ln 2},$$

where $e_1 = \|\phi_f - \phi_e\|$ and $e_2 = \|\phi_c - \phi_e\|$ and ϕ_e, ϕ_f and ϕ_c are, respectively, exact, fine grid, and coarse grid solutions. We use $\beta = 100$, $Re = 100$ and $CFL = 10$. Table 1 shows the errors and numerical orders of accuracy. We observe that the modified scheme has almost the same errors as the original scheme and the third-order accuracy in L_∞ and L_2 norms.

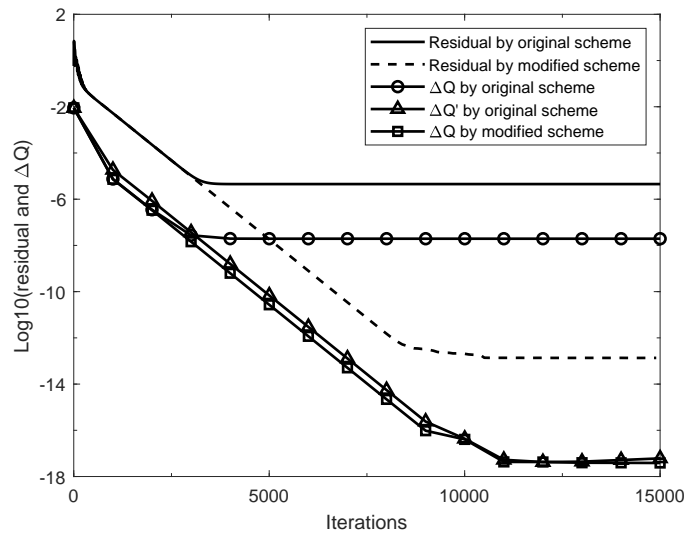


Figure 5: Convergence of the original and modified schemes for modified lid-driven cavity flow, $Re = 100$, $\beta = 100$, $CFL = 10$, 81×81 grid points.

Table 1: Accuracy test for modified lid-driven cavity, $\beta = 100$, CFL = 10, $Re = 100$.

Grid	Original upwind compact scheme				Modified upwind compact scheme			
	L_∞ error	Order	L_2 error	Order	L_∞ error	Order	L_2 error	Order
11^2	3.74E-2	—	1.02E-2	—	3.69E-2	—	1.01E-2	—
21^2	4.64E-3	3.01	1.38E-3	2.89	4.75E-3	2.96	1.37E-3	2.88
41^2	5.93E-4	2.97	1.79E-4	2.95	5.96E-4	2.99	1.79E-4	2.94
81^2	7.39E-5	3.00	2.29E-5	2.97	7.39E-5	3.01	2.29E-5	2.97
161^2	9.20E-6	3.00	2.90E-6	2.98	9.22E-6	3.00	2.90E-6	2.98
321^2	1.16E-6	2.99	3.74E-7	2.95	1.16E-6	2.99	3.74E-7	2.95

The convergence of the two schemes for this problem is displayed in Fig. 5. The residuals and solution increments of the modified upwind compact scheme converge to machine accuracy, but those of the original upwind compact scheme stop at large magnitudes. On the other hand, machine zero convergence of the modified increments $\Delta \mathbf{Q}'$ for the original upwind compact scheme guarantees the expected accuracy — cf. Section 3.2 and Table 1.

5.2. Lid-driven cavity flow

This flow is driven by the translation of the top lid. As the Reynolds number increases, there appear numerous complicated separation vortices at the corners. We set $Re = 100$, 400, 1000, 5000 for which stationary solutions exist. The boundary and initial conditions are the same as in Section 3.1. We use $\beta = 10$ and 129×129 uniform grid points. Fig. 6 shows the convergence of the original and modified schemes for $Re = 5000$. We again

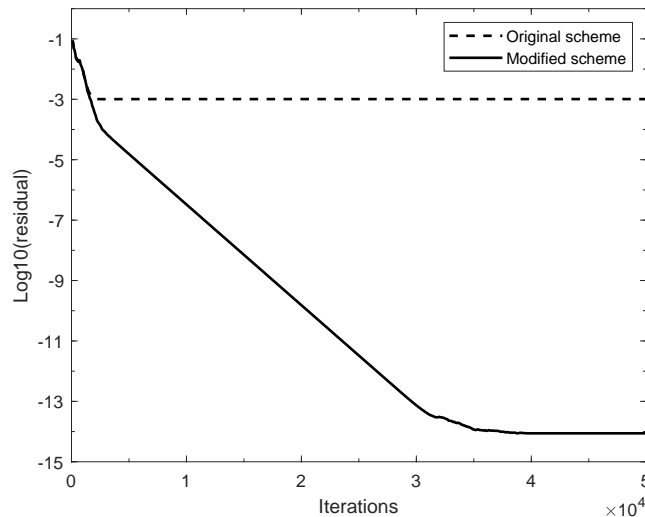


Figure 6: Comparison of convergence histories for lid-driven cavity flow between two schemes. $Re = 5000$, $\beta = 1$, CFL = 20, 129×129 grid points.

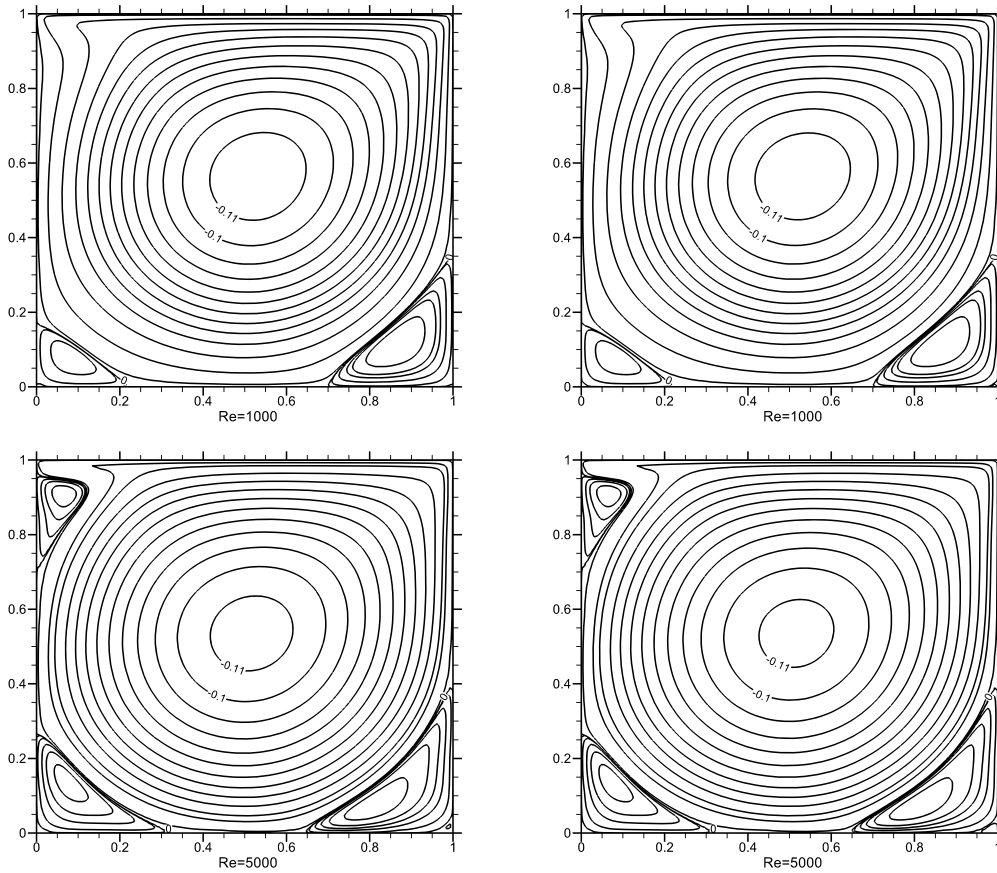


Figure 7: Streamlines for lid-driven cavity flow at $Re = 1000$ and $Re = 5000$ computed with the original scheme (left) and modified scheme (right) on the 129×129 grid, $CFL = 10$, $\beta = 10$.

note that the modified scheme converges to machine zero but the original scheme gets flat at a higher level. The streamlines of the modified scheme shown in Fig. 7 agree with the results [9, 14].

Fig. 8 demonstrates the velocity components u and v on the lines crossing the center of the cavity along the y and x axes. The results of modified and original schemes well agree with each other and with the classical numerical results of Ghia *et al.* [14].

Table 2 contains minimum of u -velocity along $x = 0.5$ and maximum of v -velocity along $y = 0.5$ determined by the original and modified schemes and by [14, 36, 42]. For $Re \leq 1000$, the results agree with each other and with the reference results. Only for $Re = 5000$ the results from different sources differ.

5.3. Rectangular cavity flow

The lid-driven flows in rectangular cavity with various depth-to-width ratios ($D = H/L$) have the same boundary conditions as the lid-driven cavity flow with $D = 1$. The previous

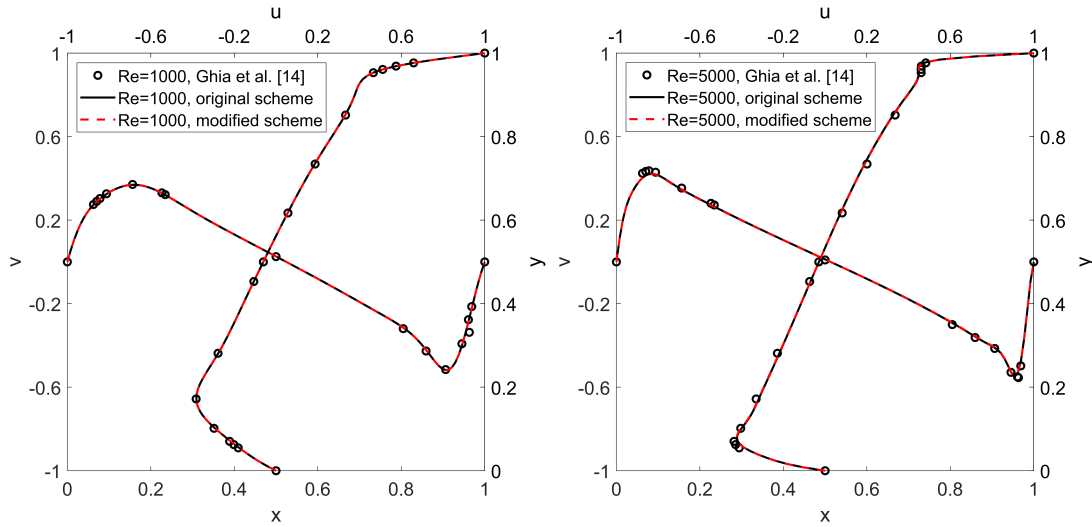


Figure 8: Velocity profiles of lid-driven cavity flow determined by [14], the original and modified schemes, $Re = 1000$ and 5000 .

Table 2: Lid-driven cavity flow. Minimum of u -velocity along $x = 0.5$ and y -coordinate y_{min} , maximum of v -velocity along $y = 0.5$ and x -coordinate x_{max} .

Re	Source	Grid size	u_{min}	y_{min}	v_{max}	x_{max}
100	Original scheme	129×129	-0.21146	0.4609	0.17552	0.2344
	Modified scheme	129×129	-0.21144	0.4609	0.17750	0.2344
	Ghia <i>et al.</i> [14]	129×129	-0.21090	0.4531	0.17527	0.2344
	Sahin and Owens [36]	257×257	-0.21392	0.4598	0.18089	0.2354
400	Original scheme	129×129	-0.32420	0.2813	0.29913	0.2266
	Modified scheme	129×129	-0.32407	0.2813	0.29901	0.2266
	Ghia <i>et al.</i> [14]	129×129	-0.32726	0.2813	0.30203	0.2266
	Sahin and Owens [36]	257×257	-0.32838	0.2815	0.30445	0.2253
1000	Original scheme	129×129	-0.38175	0.1719	0.36974	0.1563
	Modified scheme	129×129	-0.38141	0.1719	0.36957	0.1563
	Ghia <i>et al.</i> [14]	129×129	-0.38289	0.1719	0.37095	0.1563
	Sahin and Owens [36]	257×257	-0.38810	0.1727	0.37691	0.1573
	Tian <i>et al.</i> [42]	257×257	-0.38373	0.1719	0.37181	0.1602
5000	Original scheme	129×129	-0.42247	0.0781	0.42076	0.0859
	Modified scheme	129×129	-0.42162	0.0781	0.41939	0.0859
	Ghia <i>et al.</i> [14]	129×129	-0.43643	0.0703	0.43648	0.0781
	Sahin and Owens [36]	257×257	-0.43590	0.0664	0.42590	0.0762
	Tian <i>et al.</i> [42]	257×257	-0.43050	0.0938	0.42703	0.0977

works [4,26] focus on the influence of D and Re on the flow structure. Here we simulate two cases $D = 2.2$ and $D = 2.4$ for the same $Re = UL/\nu = 1000$. Moreover, $\beta = 10$, $CFL = 30$, and 129×257 uniform grid points are used so that grid sizes $\Delta x \neq \Delta y$ are intentionally

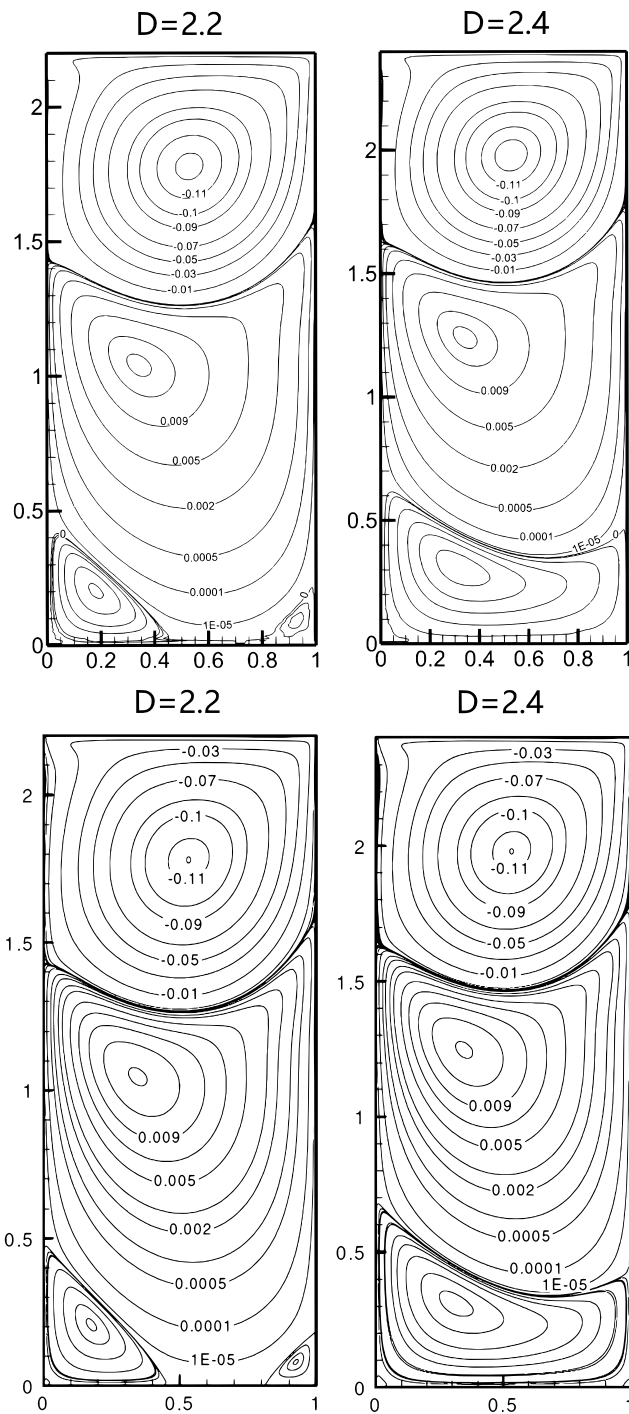


Figure 9: Comparison of streamlines for rectangular cavity flows with $D = 2.2$ and 2.4 at $Re = 1000$ between the modified scheme results on uniform 129×257 grid with $\beta = 10$, $CFL = 30$ (upside) and the lattice Boltzmann results on the $201 \times 201D$ grid [4] (downside).

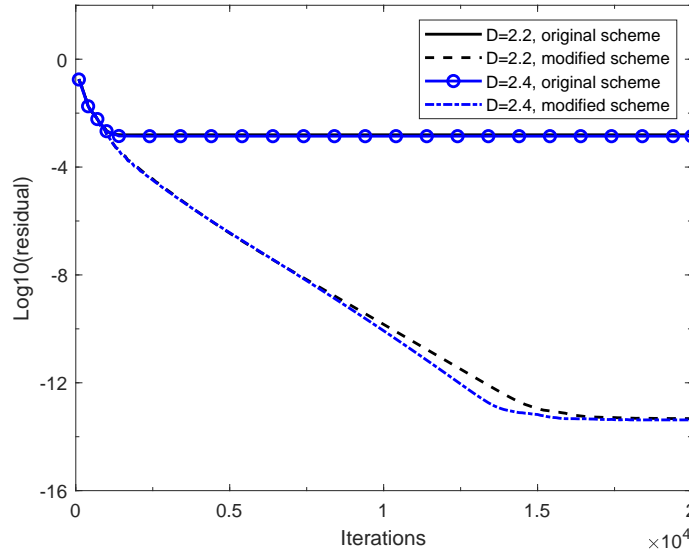


Figure 10: Comparison of residual histories for two rectangular cavity flows at $Re = 1000$ between the original and modified schemes with 129×257 grid points, $\beta = 10$, $CFL = 30$.

arranged in order to see if the modified scheme works for such a setup. Fig. 9 shows that the current streamline results agree with [4] and Fig. 10 demonstrates the residuals in the modified scheme converge to machine zero while those in the original scheme get flat.

5.4. Backward facing step flow

The flow over a backward facing step is a benchmark problem for testing incompressible flow solvers. In spite of a simple geometry, the backward facing step flow features separations, reattachments, recirculations and shear layers [1, 12, 19, 23]. We use the computational domain shown in Fig. 11. The upstream channel provides a fully developed parabolic velocity profile at the inlet. Non-slip boundary conditions for the velocity and the Neumann boundary conditions for the pressure derived from the normal-to-wall momentum equation are used on all walls. The velocity of the incoming flow

$$u = 12y(1 - 2y), \quad v = 0, \quad y \in [0, 0.5]$$

was considered [38]. The pressure at the inlet is extrapolated from the interior. The coordinate is normalised by the channel width $h = 1$ at the step, and the velocity is normalised by the mean velocity $\bar{V} = 1$ at the inlet. The origin of the x, y coordinates is at the upper corner point of the step. The outflow boundary consists of zero normal derivative for the velocity and zero pressure.

This is an open domain flow problem and we use the original upwind compact scheme to compute it. The computational domain $[0, 31h] \times [0, h]$ is gridded with uniform 311×101 grid points — cf. Fig. 11, and $\beta = 10$ and $CFL = 10$ are used. The initial conditions

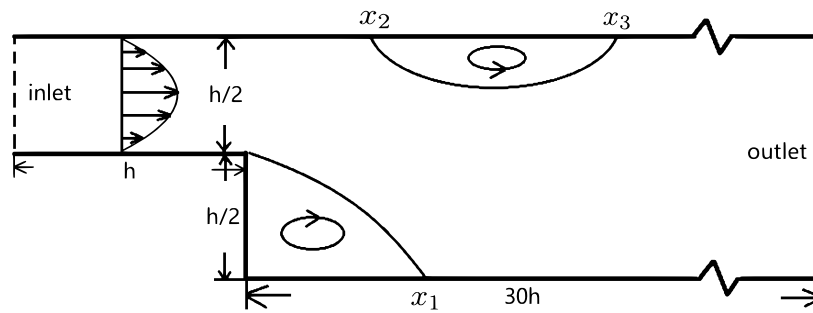


Figure 11: Geometry of backward facing step flow problem.

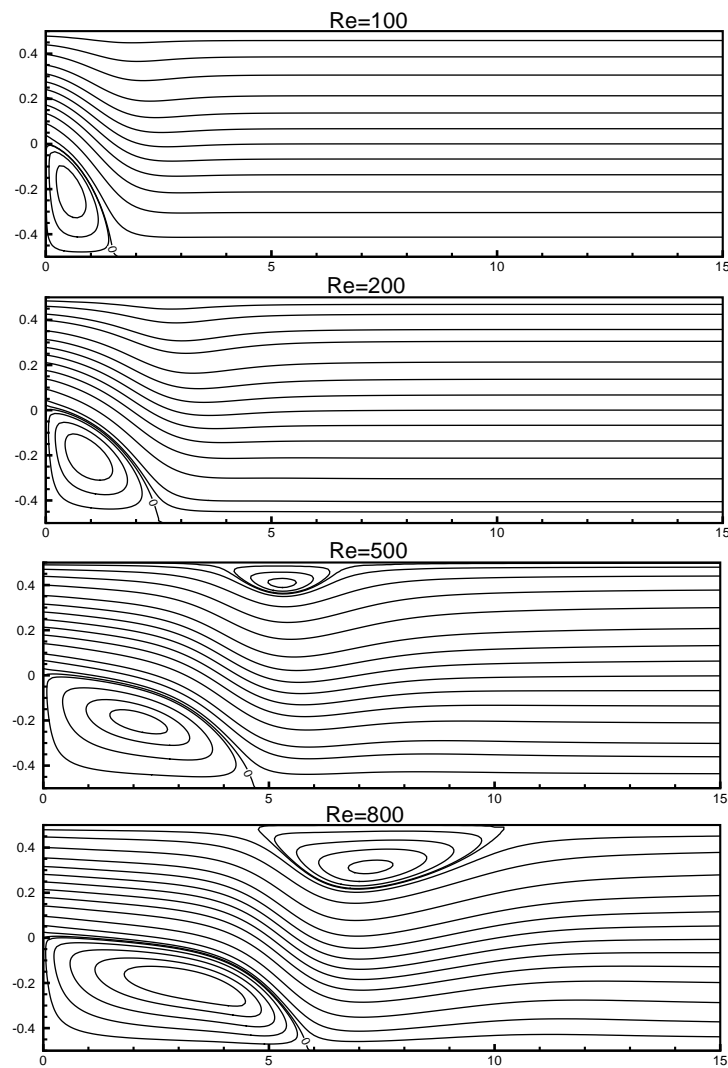


Figure 12: Streamlines of backward facing step flow at different Reynolds numbers. The x scale is reduced by $1/5$ for visibility.

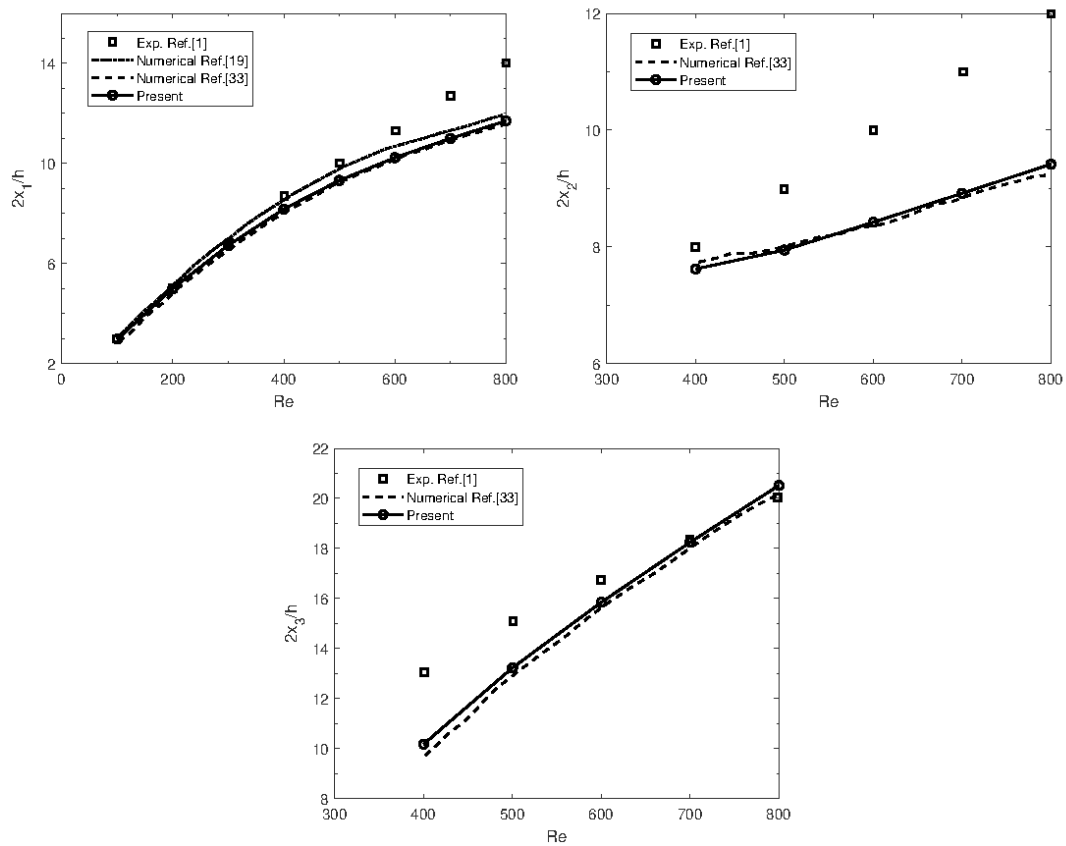


Figure 13: Comparison of non-dimensional separation and reattachment lengths of backward facing step flow problem between the present and experimental [1] and previous numerical results [19, 33].

are specified as $u = 1, v = 0$ at the interior points with zero pressure everywhere. To be consistent with the literature, the Reynolds number below is defined as $Re = \overline{V}D/\nu$, where $\overline{V} = 1$ is two thirds of the maximum inlet velocity, D the hydraulic diameter of the inlet (small) channel equivalent to twice its height — i.e. $D = h$.

Fig. 12 shows the streamlines for different Reynolds numbers. We observe that the separation bubble grows with the steps and another one occurs on the upper wall when Reynolds number increases. Fig. 13 compares the separation and reattachment points x_1, x_2, x_3 as defined in Fig. 11 with the experimental results [1] and the simulation results [19, 33]. Note that present and other numerical results agree with each others but disagree with experiments, particularly for the separation point x_2 on the upper wall. The difference between the experimental results and numerical results may be due to possible 3D effects in the experiments.

Fig. 14 shows the u -velocity profiles at $x/2h = 7$ and $x/2h = 15$ for $Re = 800$. The present numerical results agree with the numerical results of Gartling [12] who did not include the upstream channel in his computation.

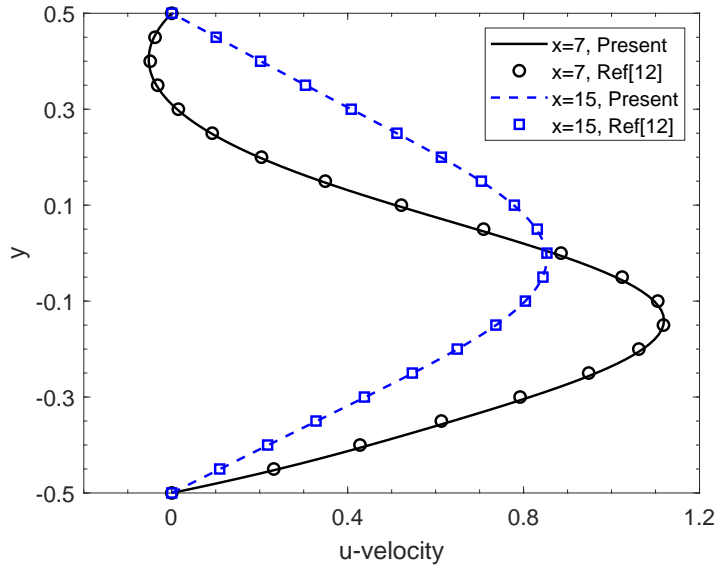


Figure 14: Horizontal velocity profiles along the height of the channel at two x positions for backward-facing step flow at $Re = 800$ in comparison with the numerical results [12].

5.5. Spherical Couette flow

Finally, the three-dimensional spherical Couette flow (SCF) between two concentric rotating spheres is simulated. In the present setup, the inner sphere rotates and the outer is fixed. As the Reynolds number grows, Taylor-Görtler (TG) vortices occur [24, 45, 46] in the form of toroidal vortices. For a medium gap width ratio $\sigma = (R_2 - R_1)/R_1 = 0.18$, stationary solutions exist for $Re < 1220$ [45]. As a flow in enclosed domain the SCF is used to test the modified scheme in 3D situation.

Fig. 15 demonstrates the computational domain composed of the whole spherical gap $(\theta, \phi, r) = [0, \pi] \times [0, 2\pi] \times [R_1, R_2]$. It is discretised by $361(\theta) \times 129(\phi) \times 31(r)$ grid points. The grid points along the r direction are clustered toward both spherical walls. The governing equations written in the generalised curvilinear coordinates ξ, η and ζ [46] are solved, where ξ, η and ζ are along the θ, ϕ and r directions respectively. Non-slip conditions for the velocity and Neumann boundary conditions for the pressure derived from the r -direction momentum equation in the spherical coordinates are applied on both inner and outer spheres. On the poles $\theta = 0$ and $\theta = \pi$, axial symmetry conditions are assumed. In the ϕ direction, periodic boundary conditions are used. The modification (4.4) is used in all the three directions.

We calculate steady flows at $Re = 600$, $Re = 700$ and $Re = 800$ with $CFL = 10$, $\beta = 1.0$ and obtain a subcritical 0- and supercritical 1- and 2-vortex flows — cf. Fig. 16. These flow modes are similar to the numerical ones [24, 46]. The residuals are shown in Fig. 17. We observe that the residuals of the original scheme get flat at a high level, but the ones calculated with the modified scheme converge to machine zero. It is remarked that the

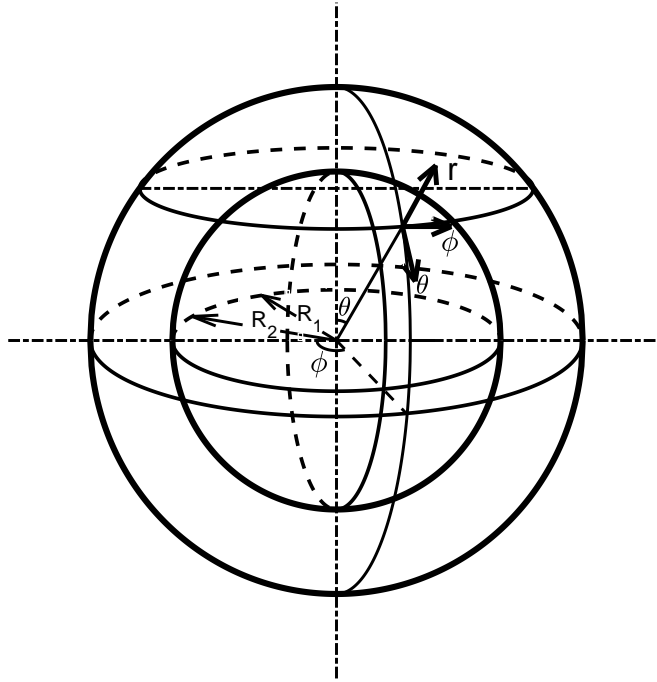


Figure 15: Geometry of spherical Couette flow.

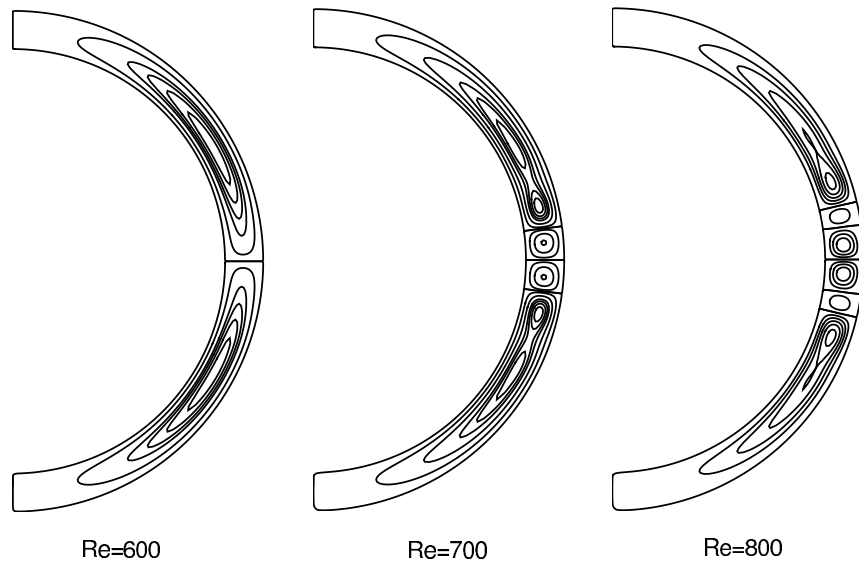


Figure 16: Contours of the meridional streamfunction for 0-, 1- and 2-vortex flows with a gap width $\sigma = 0.18$ obtained by the modified scheme with $CFL = 10$, $\beta = 1$ and $361 \times 129 \times 31$ grid points.

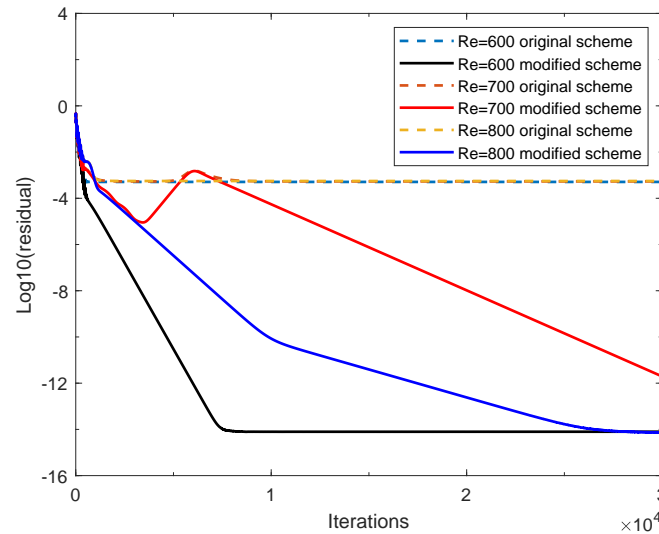


Figure 17: Convergence of original and modified schemes for spherical Couette flow, $\sigma = 0.18$, $Re = 800$, CFL= 10, $\beta = 1$, $361 \times 129 \times 31$ grid points.

formation of 1-vortex flow at $Re = 700$ undergoes a symmetry-breaking process so the convergence is slower than other two cases. Specifically, the SCF with $\sigma = 0.18$ is linearly unstable for $651 \leq Re \leq 775$ [24]. This instability makes the equator symmetry break (marked by a temporary rise in the residual from 4000 to 6100 iterations), and after that the flow gradually recovers the equatorial symmetry in a long time.

6. Conclusion

We study the residual stall issues associated with a third-order flux difference splitting based upwind compact scheme for incompressible steady flows in enclosed domains. It is shown that the residuals got flat since the calculated pressure is unique only up to a time-dependent constant when Neumann boundary conditions for the pressure are imposed on all boundaries, and this varying constant can not make the time derivative of pressure in the continuity equation of the AC method vanish. This deficiency can be fixed by modifying the calculated derivatives of the mass flux to satisfy the global mass conservation in enclosed domain. Numerical results show that with this modification the upwind compact scheme converges to machine accuracy and holds the original order of accuracy. The modification can be implemented in other numerical schemes exploiting the AC method.

Acknowledgments

This work is supported by Natural Science Foundation of China (Grant Nos. 91641107, 91852116, 12071470). The computations are carried out on high performance computers

of the State Key Laboratory of Scientific and Engineering Computing, Chinese Academy of Sciences.

References

- [1] B. Armaly, F. Durst, J. Pereira, and B. Schönung, *Experimental and theoretical investigation of backward-facing step flow*, *J. Fluid Mech.* **127**, 473–496 (1983).
- [2] M. Athavale and C. Merkle, *An upwind differencing scheme for time-accurate solutions of unsteady incompressible flow*, AIAA Paper 88–3650 (1988).
- [3] P.T. Brady and D. Livescu, *High-order, stable, and conservative boundary schemes for central and compact finite differences*, *Comput. & Fluids* **183**, 84–101 (2018).
- [4] M. Cheng, K.C. Hung, *Vortex structure of steady flow in a rectangular cavity*, *Comput. & Fluids* **35**, 1046–1062 (2006).
- [5] D. Choi and C. Merkle, *Application of time-iterative schemes to incompressible flow*, *AIAA Journal* **23**, 1518–1524 (1985).
- [6] A. Chorin, *Numerical method for solving incompressible viscous flow problems*, *J. Comput. Phys.* **2**, 12–26 (1967).
- [7] X.G. Deng, *High-order accurate dissipative weighted compact nonlinear schemes*, *Science in China Ser. A* **45**, 356–370 (2002).
- [8] J. Ekaterinaris, *High-order accurate numerical solutions of incompressible flows with the artificial compressibility method*, *Int. J. Numer. Meth. Fluids* **45**, 1187–1207 (2004).
- [9] E. Erturk, T. Corke, and C. Gökçöl, *Numerical solutions of 2-D steady incompressible driven cavity flow at high Reynolds numbers*, *Int. J. Numer. Meth. Fluids* **48**, 747–774 (2005).
- [10] J.H. Ferziger and M. Peric, *Computational Methods for Fluid Dynamics*, Springer (2002).
- [11] D.X. Fu and Y.W. Ma, *A high order accurate difference scheme for complex flow fields*, *J. Comput. Phys.* **134**, 1–15 (1997).
- [12] D. Gartling, *A test problem for outflow boundary conditions-flow over a backward-facing step*, *Int. J. Numer. Meth. Fluids* **11**, 953–967 (1990).
- [13] R. Gatiganti, K. Badcock, F. Cantariti, L. Dubuc, M. Woodgate, and B. Richards, *Evaluation of an unfactored method for the solution of the incompressible flow equations using artificial compressibility*, *Applied Ocean Research* **20**, 179–187 (1998).
- [14] U. Ghia, K.N. Ghia, and C. Shin, *High-Re solutions for incompressible flow using the Navier-Stokes equations and a multigrid method*, *J. Comput. Phys.* **48**, 387–411 (1982).
- [15] P. Hartwich and C. Hsu, *High resolution upwind schemes for the three-dimensional incompressible Navier-Stokes equations*, *AIAA Journal* **26**, 1321–1332 (1988).
- [16] A. Jameson, *Time dependent calculations using multigrid with applications to unsteady flows past airfoils and wings*, AIAA Paper 91–1596 (1991).
- [17] L. Jiang, H. Shan, and C.Q. Liu, *Weighted compact scheme for shock capturing*, *Int. J. Comput. Fluid Dyn.* **15**, 147–155 (2001).
- [18] G.S. Jiang, C.-W. Shu, *Efficient implementation of weighted ENO schemes*, *J. Comput. Phys.* **126**, 202–228 (1996).
- [19] J. Kim and P. Moin, *Application of a fractional-step method to incompressible Navier-Stokes equations*, *J. Comput. Phys.* **59**, 308–323 (1985).
- [20] D. Kwak, J. Chang, S. Shanks, and S. Chakravarthy, *A three-dimensional incompressible Navier-Stokes flow solver using primitive variables*, *AIAA Journal* **24**, 390–396 (1986).
- [21] D. Kwak, C. Kiris, and J. Housman, *Implicit methods for viscous incompressible flows*, *Comput. & Fluids* **41**, 51–64 (2011).

- [22] S. Lele, *Compact finite difference schemes with spectral-like resolution*, J. Comput. Phys. **103**, 16–42 (1992).
- [23] Z.Q. Li and R. Wood, *Accuracy verification of a 2D adaptive mesh refinement method for incompressible or steady flow*, J. Comput. Appl. Math. **318**, 259–265 (2016).
- [24] P.S. Marcus and L.S. Tuckerman, *Simulation of flow between concentric rotating spheres. Part 1. Steady states*, J. Fluid Mech. **185**, 1–30 (1987).
- [25] M. Napolitano, *A Fortran subroutine for the solution of periodic block-tridiagonal systems*, Commun. Numer. Methods Eng. **1**, 11–15 (1985).
- [26] F. Pan, A. Acrivos, *Steady flows in rectangular cavities*, J. Fluid Mech. **28**, 643–655 (1967).
- [27] S. Pirozzoli, *Conservative hybrid compact-WENO schemes for shock-turbulence interaction*, J. Comput. Phys. **178**, 81–117 (2002).
- [28] Y.X. Ren, M.R. Liu, and H.X. Zhang, *A characteristic-wise hybrid compact-WENO scheme for solving hyperbolic conservation laws*, J. Comput. Phys. **92**, 365–386 (2003).
- [29] M. Rizwan, A. Shah, and L. Yuan, *A central compact scheme for numerical solution of two-phase incompressible flow using Allen-Cahn phase field model*, J. Braz. Soc. Mech. Sci. Eng. **38**, 433–441 (2016).
- [30] P.L. Roe, *Approximate Riemann solvers, parameter vectors, and difference scheme*, J. Comput. Phys. **43**, 357–372 (1981).
- [31] S. Rogers, *A comparison of implicit schemes for the incompressible Navier-Stokes equations and artificial compressibility*, AIAA Journal **33**, 2066–72 (1995).
- [32] S. Rogers, J. Chang, and D. Kwak, *A diagonal algorithm for the method of pseudocompressibility*, J. Comput. Phys. **73**, 364–379 (1987).
- [33] S. Rogers and D. Kwak, *An upwind differencing scheme for the incompressible Navier-Stokes equations*, Appl. Numer. Math. **8**, 43–64 (1991). (also NASA TM 101051, 1988).
- [34] S. Rogers and D. Kwak, *An upwind differencing scheme for the time-accurate incompressible Navier-Stokes equations*, AIAA Journal **28**, 253–262 (1990).
- [35] S. Rogers, D. Kwak, and C. Kiris, *Numerical solution of the incompressible Navier-Stokes equations for steady-state and time-dependent problems*, AIAA Journal **29**, 603–610 (1991).
- [36] M. Sahin and R.G. Owens, *A novel fully implicit finite volume method applied to the lid-driven cavity problem-Part I: High Reynolds number flow calculations*, Int. J. Numer. Meth. Fluids **42**, 57–77 (2003).
- [37] A. Shah, H. Guo, and L. Yuan, *A third-order upwind compact scheme on curvilinear meshes for the incompressible Navier-Stokes equations*, Commun. Comput. Phys **5**, 712–729 (2009).
- [38] A. Shah and L. Yuan, *Flux-difference splitting-based upwind compact schemes for the incompressible Navier-Stokes equations*, Int. J. Numer. Meth. Fluids **61**, 52–568 (2009).
- [39] A. Shah, L. Yuan, and A. Khan, *Upwind compact finite difference scheme for time-accurate solution of the incompressible Navier-Stokes equations*, Appl. Math. Comput. **215**, 3201–3213 (2010).
- [40] T. Shih, C. Tan, and B. Hwang, *Effects of grid staggering on numerical schemes*, Int. J. Numer. Meth. Fluids **9**, 193–212 (1989).
- [41] W. Soh and J. Goodrich, *Unsteady solution of incompressible Navier-Stokes equations*, J. Comput. Phys. **79**, 113–134 (1988).
- [42] Z.F. Tian, X. Liang, and P. Yu, *A higher order compact finite difference algorithm for solving the incompressible Navier-Stokes equations*, Int. J. Numer. Meth. Engineering **88**, 511–532 (2011).
- [43] M. Visbal and D. Gaitonde, *On the use of higher-order finite-difference schemes on curvilinear and deforming meshes*, J. Comput. Phys. **181**, 155–185 (2002).
- [44] S. Yoon, D. Kwak, *LU-SGS implicit algorithm for three-dimensional incompressible Navier-Stokes equations with source term*, AIAA Paper 89–1964 (1989).

- [45] L. Yuan, *Numerical investigation of wavy and spiral Taylor-Görtler vortices in medium spherical gaps*, *Physics of Fluids* **24**, 124104 (2012).
- [46] L. Yuan, D.X. Fu, and Y.W. Ma, *Numerical study of bifurcation solutions of spherical Taylor-Couette flow*, *Science in China Ser. A* **39**, 187–196 (1996).
- [47] J.B. Zhang and Z.S. Qian, *Implicit eighth-order central compact scheme for the numerical simulation of steady and unsteady incompressible Navier-Stokes equations*, *Int. J. Comput. Fluid Dyn.* **26**, 247–261 (2012).
- [48] F. Zhang, H.S. Tang, J. Cheng, and T.G. Liu, *A simplified artificial compressibility flux for the discontinuous Galerkin solution of the incompressible Navier-Stokes equations*, *Commun. Comput. Phys.* **25**, 988–1009 (2019).